

## Mapping of Io's thermal radiation by the Galileo photopolarimeter–radiometer (PPR) instrument

J.A. Rathbun,<sup>a,b,\*</sup> J.R. Spencer,<sup>b</sup> L.K. Tamppari,<sup>c</sup> T.Z. Martin,<sup>c</sup> L. Barnard,<sup>d</sup> and L.D. Travis<sup>e</sup>

<sup>a</sup> *University of Redlands, 1200 East Colton Avenue, PO Box 3080, Redlands, CA 92373, USA*

<sup>b</sup> *Lowell Observatory, 1400 West Mars Hill Road, Flagstaff, AZ 86001, USA*

<sup>c</sup> *Jet Propulsion Laboratory, 4800 Oak Grove Drive, Pasadena, CA 91109, USA*

<sup>d</sup> *Raytheon Corporation, 299 S. Euclid Avenue, Pasadena, CA 91109, USA*

<sup>e</sup> *NASA-GISS, 2880 Broadway, New York, NY 10025, USA*

Received 4 February 2003; revised 16 December 2003

### Abstract

Between 1999 and 2002, the Galileo spacecraft made 6 close flybys of Io during which many observations of Io's thermal radiation were made with the photopolarimeter–radiometer (PPR). While the NIMS instrument could measure thermal emission from hot spots with  $T > 200$  K, PPR was the only Galileo instrument capable of mapping the lower temperatures of older, cooling lava flows, and the passive background. We tabulate all data taken by PPR of Io during these flybys and describe some scientific highlights revealed by the data. The data include almost complete coverage of Io at better than 250 km resolution, with extensive regional coverage at higher resolutions. We found a modest poleward drop in nighttime background temperatures and evidence of thermal inertia variations across the surface. Comparison of high spatial resolution temperature measurements with observed daytime SO<sub>2</sub> gas pressures on Io provides evidence for local cold trapping of SO<sub>2</sub> frost on scales smaller than the 60 km resolution of the PPR data. We also calculated the power output from several hot spots and estimated total global heat flow to be about 2.0–2.6 W m<sup>−2</sup>. The low-latitude diurnal temperature variations for the regions between obvious hot spots are well matched by a laterally-inhomogeneous thermal model with less than 1 W m<sup>−2</sup> endogenic heat flow.

© 2004 Elsevier Inc. All rights reserved.

**Keywords:** Io; Volcanism; Infrared observations; Surfaces, satellites; Thermal histories

### 1. Introduction

Io, the closest galilean satellite to Jupiter, is the most volcanically active body in the Solar System. The Galileo spacecraft has been studying the Jupiter system since 1995 and between 1999 and 2002 made 6 close flybys of Io. Three remote sensing instruments are particularly useful in studying the active volcanism on Io: The solid-state imager (SSI), near-infrared mapping spectrometer (NIMS), and photopolarimeter–radiometer (PPR). Of these, PPR is the simplest (it is a single aperture photometer) and has the lowest spatial resolution (2.5 mrad) but, since it is sensitive from visible wavelengths up to 100 μm (Russell et al., 1992), it is the only instrument that can detect thermal radiation from surfaces colder than 200 K, such as low-temperature hotspots and the passive (sun-heated) surface

between the hot spots. Here we describe all of the data taken by PPR at Io during the close flybys, and highlight some of the principle scientific results obtained from these data.

Though PPR can obtain visible-wavelength photometry and polarization data (Martin et al., 2000) at Io PPR was most often used in radiometry mode, in which the instrument operates in the thermal infrared. When it is the primary instrument, PPR usually builds up images by raster-scanning the Galileo scan platform across its target. When used in “ride-along” mode, in conjunction with another remote sensing instrument (either SSI or NIMS), PPR generally produces one-dimensional temperature scans. Three different filters were used for Io radiometry: a “17 μm” filter, covering the range 14.7–18.9 μm, used during some of the ride-along observations; a “27 μm” filter, covering the range 24.1–32.3 μm, usually used for dayside images; and an open filter, which is sensitive to radiation from the visible to 100 μm. The open filter is by far the most sen-

\* Corresponding author.

E-mail address: [julie\\_rathbun@redlands.edu](mailto:julie_rathbun@redlands.edu) (J.A. Rathbun).

sitive filter for temperature mapping, but cannot be used for daytime observations because it cannot distinguish thermal radiation from reflected sunlight. It was thus normally used for nightside observations. Some nighttime observations included a flux contribution from reflected Jupiter light, which we estimate (Spencer et al., 2000a) resulted in an overestimation of temperature of  $< 2$  K. Observed flux in the discrete filters is most conveniently expressed as brightness temperature ( $T_B$ ), which is the temperature of a blackbody emitting the observed flux at the observed wavelength. For the open filter, what we call brightness temperature is really effective temperature, defined as the temperature of a blackbody radiating the observed power at all wavelengths. Caution should be exercised in converting brightness temperatures to physical surface temperatures, especially for Io whose thermal emission spectrum deviates significantly from a blackbody (Spencer et al., 2003) due to both unresolved temperature contrasts within the field of view of most observations, resulting from local variations in albedo, thermal inertia, or volcanic heat (McEwen et al., 1992, 1996), and spectral features due to non-unit emissivity which varies with wavelength due to spectrally-active surface species (Khanna et al., 1995). The flux is sampled and recorded at intervals of 0.46 seconds throughout an observation.

Radiation noise was a significant problem at Io, with noise levels several times higher than those seen at the orbits of Callisto or Ganymede, but could be reduced by averaging samples, and did not prevent useful observations. For example, one of our highest noise observations, the 27  $\mu\text{m}$  observation 31IPDGT01 (Fig. 1), has a noise of 26 DN in the unbinned data, corresponding to  $\pm 11$  K at 120 K. Nyquist overlap of different fields of view, and subsequent smoothing of the image means that in this particular observation each point on the surface is effectively observed about 50 times, giving 7-fold noise reduction to 1.6 K at 120 K. Nighttime data taken in the open filter has lower noise levels. For instance 31IPNSDR01 (Fig. 6) has a noise level of 6 DN before binning, corresponding to  $\pm 3$  K at 95 K. The scan rate for this observation covered the 2.5 mrad PPR field of view in 30 0.46 second samples, so binning by 15 samples, for Nyquist sampling, reduced the noise level to 1.5 DN, or 0.8 K.

Radiometric calibration of PPR data was checked using periodic observations of an on-board blackbody (the radiometric calibration target) of known temperature. PPR uses a chopper to rapidly compare observations of the sky with observations of the target, and drifts in internal temperature can sometimes produce spurious offsets of a few data numbers (DN) in the signal between the two beams. These offsets can be detected as non-zero DNs seen when looking at the sky off the limb of our targets.

Galileo orbits are generally described by a letter, which indicates the satellite Galileo flew closest to on that orbit, such as “I” for Io, followed by a number indicating the sequential number of that orbit. Excluding a close flyby of

Io prior to Jupiter orbit insertion, when no remote sensing data were obtained, Galileo’s Io flybys were I24, which took place October 10, 1999, I25 (November 25, 1999), I27 (February 22, 2000), I31 (August 5, 2001), I32 (October 15, 2002), and I33 (January 17, 2003). PPR was the only instrument to gather remote sensing data on I33, due to a spacecraft anomaly.

PPR data are archived in the form of a pair of ASCII data tables for each observation, giving the radiometric and geometric information for each 0.46 second sample. All data will shortly be available at the Planetary Data System Atmosphere Node (<http://atmos.nmsu.edu/atmos-home.html>), and can also be obtained from <http://www.lowell.edu/users/ppr/>.

Brightness temperatures measured by PPR can be used in a variety of ways, some of which we begin to address in this paper. They can be used to study active volcanism and are particularly useful for measuring cooler lava flows near or below the  $\sim 200$  K detection limit of NIMS (Carlson et al., 1992). From the flow’s temperature, its age can be calculated from simple lava cooling models (e.g., Howell, 1997). The total power from a volcanic hotspot can be calculated from its signal in the open filter when the hotspot is not resolved. Because the open filter detects all radiation emitted by Io, open filter observations are useful for estimating Io’s total heat budget and endogenic heat flow. Passive surface temperature measurements constrain  $\text{SO}_2$  frost temperatures, which are an important influence on atmospheric density and dynamics. The thermal inertia and other surface properties can be estimated from diurnal temperature variations.

## 2. Data

The PPR instrument obtained more than 100 observations of Io during the close flybys between 1999 and 2002. Table 1 lists all PPR data of Io obtained in orbits I24 through I33. The observation name gives some information about the observation: the 2-digit orbit number is followed by the target (always “I” for Io in this case), the primary instrument (the instrument with primary control of the spacecraft pointing—“P” for PPR, “S” for SSI, and “N” for NIMS), and an 8-character name and number describing the observation. The table also gives the average resolution of the observation (which gives some indication of the extent of the observation), the average time of day (in degrees, defined as 0 at midnight, 90 at sunrise, and 180 at noon), the average longitude and latitude, the total temperature range measured in the observation (large numbers indicate the presence of hotspots in the data), the duration of the observation, a description of the target, the time to closest approach (negative for before, positive for after) and the central wavelength of the filter used (in  $\mu\text{m}$ , with “O” indicating the open filter).

Table 1  
Galileo PPR observation of Io

| Observation name | Res. (km) | Time of day | Lon. | Lat. | $\Delta T$ | Duration | Target     | Time to C/A | $\lambda$ ( $\mu\text{m}$ ) |
|------------------|-----------|-------------|------|------|------------|----------|------------|-------------|-----------------------------|
| 24iploki_02      | 34        | 27          | 172  | 18   | 0          | 0:38:25  | Loki       | −0:50:37    | 17                          |
| 24inpele_01      | 8         | 32          | 308  | 13   | 39         | 0:01:21  | Pele       | −0:04:06    | 17                          |
| 24ispele_01      | 4         | 84          | 257  | −18  | 69         | 0:00:46  | Pele       | −0:02:45    | 17                          |
| 24ispillan01     | 2         | 99          | 242  | −10  | 58         | 0:01:01  | Pillan     | −0:01:50    | 17                          |
| 24inpillan01     | 2         | 100         | 241  | −10  | 31         | 0:02:05  | Pillan     | −0:00:49    | 17                          |
| 24iscolchs01     | 2         | 126         | 215  | 4    | 34         | 0:01:48  | Colchis    | 0:01:17     | 17                          |
| 24incolchs01     | 3         | 129         | 212  | 4    | 45         | 0:01:11  | Colchis    | 0:03:05     | 17                          |
| 24iszamama01     | 5         | 169         | 173  | 18   | 33         | 0:02:50  | Zamama     | 0:04:17     | 17                          |
| 24inzamama01     | 6         | 172         | 170  | 17   | 38         | 0:01:58  | Zamama     | 0:07:08     | 17                          |
| 24ispromth01     | 30        | 190         | 242  | −10  | 0          | 0:06:17  | Prometheus | 0:09:07     | 17                          |
| 24inpromth01     | 38        | 192         | 225  | −13  | 0          | 0:02:44  | Prometheus | 0:15:25     | 17                          |
| 24iscolchs02     | 21        | 130         | 213  | 5    | 4          | 0:01:17  | Colchis    | 0:18:10     | 17                          |
| 24incolchs02     | 23        | 129         | 214  | 3    | 7          | 0:02:07  | Colchis    | 0:19:27     | 17                          |
| 24istohil_01     | 23        | 182         | 162  | −28  | 52         | 0:01:41  | Tohil      | 0:21:35     | 17                          |
| 24inntohil01     | 26        | 186         | 159  | −26  | 0          | 0:03:10  | Tohil      | 0:23:17     | 17                          |
| 24ispromth02     | 30        | 190         | 155  | −12  | 16         | 0:02:29  | Prometheus | 0:26:29     | 17                          |
| 24inpromth02     | 38        | 192         | 154  | −1   | 17         | 0:11:38  | Prometheus | 0:28:59     | 17                          |
| 24iszamama02     | 48        | 152         | 195  | 25   | 64         | 0:04:34  | Zamama     | 0:40:39     | 17                          |
| 24inzamama02     | 52        | 175         | 172  | 18   | 2          | 0:03:49  | Zamama     | 0:45:13     | 17                          |
| 24isdorian01     | 55        | 171         | 177  | −2   | 0          | 0:01:23  | Dorian     | 0:49:07     | 17                          |
| 24indorian01     | 57        | 163         | 186  | −21  | 0          | 0:02:10  | Dorian     | 0:50:31     | 17                          |
| 24isamskigi01    | 62        | 242         | 107  | 21   | 67         | 0:04:34  | Amirani    | 0:52:42     | 17                          |
| 24inamskigi01    | 66        | 234         | 115  | 24   | 3          | 0:03:46  | Amirani    | 0:57:17     | 17                          |
| 24istermap01     | 71        | 260         | 90   | 1    | 0          | 0:01:41  | Terminator | 1:01:07     | 17                          |
| 24intermap01     | 73        | 254         | 96   | −5   | 0          | 0:02:01  | Terminator | 1:03:39     | 17                          |
| 24inregion01     | 130       | 207         | 150  | 4    | 5          | 0:33:22  |            | 1:36:00     | 17                          |
| 24inplume01      | 161       | 135         | 225  | −13  | 19         | 0:06:02  |            | 2:14:27     | 17                          |
| 24inpelepm01     | 263       | 147         | 224  | −18  | 6          | 0:06:04  | Pele       | 3:33:17     | 17                          |
| 24inregion02     | 529       | 201         | 194  | 8    | 28         | 0:17:11  |            | 6:10:01     | 17                          |
| 24isglocol01     | 1645      | 221         | 235  | 7    | 0          | 0:03:02  | Global     | 13:32:53    | 27                          |
| 24iseclips01     | 3725      | 226         | 177  | −2   | 0          | 0:09:06  | Global     | 23:23:22    | 27                          |
| 25ipglobal01     | 288       | 19          | 276  | 17   | 92         | 2:11:26  | Global map | −5:14:56    | O                           |
| 25isemakng02     | 36        | 219         | 119  | −4   | 21         | 0:07:13  | Emakong    | 0:32:53     | O                           |
| 25inemakng02     | 39        | 221         | 117  | −5   | 0          | 0:00:52  | Emakong    | 0:37:44     | O                           |
| 25isgiants01     |           |             |      |      | 7          | 0:05:47  | Tvashtar   | 0:40:58     | O                           |
| 25ingiants01     | 48        | 219         | 121  | 59   | 3          | 0:01:44  | Tvashtar   | 0:43:31     | O                           |
| 25isculann01     |           |             |      |      | 15         | 0:07:29  | Culann     | 0:47:02     | O                           |
| 25inculann01     | 54        | 181         | 159  | −18  | 1          | 0:00:52  | Culann     | 0:51:01     | O                           |
| 25isterm_01      |           |             |      |      | 8          | 0:04:59  | Terminator | 0:57:09     | O                           |
| 25intermap01     | 68        | 245         | 97   | 17   | 3          | 0:00:55  | Terminator | 1:01:34     | O                           |
| 25inregion01     | 86        | 197         | 147  | 6    | 8          | 0:54:36  |            | 1:04:14     | O                           |
| 27ipdrkmap01     | 344       | 22          | 240  | −5   | 67         | 1:11:47  | Global     | −6:49:08    | 27                          |
| 27iploki_01      | 116       | 350         | 308  | 9    | 156        | 1:00:40  | Loki       | −2:27:15    | O                           |
| 27ipdaedal01     | 61        | 33          | 272  | 19   | 20         | 0:39:26  | Daedalus   | −1:21:32    | O                           |
| 27iploki_02      | 30        | 358         | 312  | 11   | 205        | 0:18:12  | Loki       | −0:39:04    | O                           |
| 27iploki_03      | 15        | 1           | 311  | 12   | 198        | 0:08:05  | Loki       | −0:20:52    | O                           |
| 27inhrpele01     | 7         | 57          | 256  | −18  | 29         | 0:07:05  | Pele       | −0:11:46    | O                           |
| 27ispele_01      | 4         | 59          | 255  | −18  | 10         | 0:00:54  | Pele       | −0:05:28    | O                           |
| 27ispromth01     | 3         | 160         | 155  | −1   | 146        | 0:02:01  | Prometheus | 0:04:11     | 17                          |
| 27inmosaic01     | 18        | 160         | 157  | 13   | 12         | 0:14:02  |            | 0:11:23     | 17                          |
| 27inpromth01     | 34        | 165         | 155  | −2   | 17         | 0:10:07  | Prometheus | 0:30:42     | 17                          |
| 27istohil_01     | 41        | 160         | 160  | −28  | 14         | 0:01:27  | Tohil      | 0:40:49     | 17                          |
| 27ispromth02     | 42        | 167         | 154  | 2    | 21         | 0:02:35  | Prometheus | 0:42:16     | 17                          |
| 27iscamxt01      | 46        | 177         | 145  | 13   | 12         | 0:03:42  | Camaxtli   | 0:44:51     | 17                          |
| 27incamxt01      | 49        | 186         | 136  | 14   | 13         | 0:02:00  | Camaxtli   | 0:49:48     | 17                          |
| 27isamrani01     | 52        | 207         | 115  | 23   | 14         | 0:01:34  | Amirani    | 0:52:57     | 17                          |
| 27inamrani01     | 60        | 208         | 115  | 27   | 15         | 0:18:40  | Amirani    | 0:55:52     | 17                          |
| 27isalztrm01     | 84        | 253         | 73   | 35   | 56         | 0:03:55  | Zal        | 1:19:14     | 17                          |
| 27ipfrost_01     | 184       | 195         | 145  | −8   | 21         | 1:11:47  | Regional   | 2:24:57     | 17                          |
| 27ipdgtm_01      | 256       | 204         | 144  | 47   | 43         | 2:00:19  | Regional   | 3:34:43     | 27                          |
| 31ipglobal01     | 223       | 335         | 237  | 8    | 59         | 1:41:07  | Global     | −4:43:19    | O                           |

(continued on next page)

Table 1 (continued)

| Observation name | Res. (km) | Time of day | Lon. | Lat. | $\Delta T$ | Duration | Target         | Time to C/A | $\lambda$ ( $\mu\text{m}$ ) |
|------------------|-----------|-------------|------|------|------------|----------|----------------|-------------|-----------------------------|
| 31ippeledk01     | 145       | 332         | 252  | −25  | 104        | 1:00:40  | Pele           | −3:02:12    | O                           |
| 31ipnpolrg01     | 99        | 333         | 257  | 62   | 53         | 0:55:06  | Regional       | −2:01:36    | O                           |
| 31ipnsdrk_01     | 56        | 348         | 249  | −29  | 41         | 0:10:07  | NS scan        | −1:05:55    | O                           |
| 31iploki_01      | 40        | 291         | 308  | 13   | 152        | 0:10:07  | Loki           | −0:45:42    | O                           |
| 31ipleikng01     | 29        | 20          | 221  | 49   | 89         | 0:10:07  | Lei–Kung       | −0:35:35    | O                           |
| 31intherml01     | 14        | 347         | 256  | −19  | 93         | 0:03:00  |                | −0:32:33    | O                           |
| 31inhsum01       | 7         | 38          | 206  | 33   | 91         | 0:06:04  | Isum           | −0:11:19    | O                           |
| 31iphires_01     | 2         | 4           | 240  | 55   | 121        | 0:05:03  | Hi-res N. hem. | −0:05:15    | O                           |
| 31inso2map01     | 3         | 145         | 101  | 70   | 1          | 0:06:04  |                | 0:02:50     | O                           |
| 31intvasht01     | 19        | 124         | 124  | 62   | 62         | 0:11:07  | Tvashtar       | 0:14:58     | O                           |
| 31ingishbr01     | 40        | 162         | 89   | 17   | 8          | 0:16:09  | Gish Bar       | 0:40:11     | O                           |
| 31ipnsstrp01     | 63        | 154         | 100  | 2    | 69         | 0:17:41  | NS scan        | 0:57:22     | 27                          |
| 31inamrani01     | 85        | 139         | 119  | 23   | 38         | 0:17:11  | Amirani        | 1:20:41     | 27                          |
| 31inregion01     | 143       | 138         | 206  | 33   | 0          | 0:34:23  | Regional       | 1:51:01     | 27                          |
| 31ipdgtm_01      | 298       | 149         | 138  | −14  | 30         | 2:01:20  | Global         | 4:03:29     | 27                          |
| 32ipdrkmap01     | 639       | 331         | 194  | 5    | 18         | 0:31:21  | Global         | −11:04:25   | O                           |
| 32ipdrkmap02     | 331       | 323         | 246  | 8    | 30         | 1:07:45  | Global         | −6:08:10    | O                           |
| 32ipcolchs01     | 254       | 346         | 235  | 2    | 44         | 0:58:39  | Colchis        | −4:33:07    | O                           |
| 32ipregion01     | 193       | 333         | 257  | 33   | 57         | 0:59:39  | Regional       | −3:32:27    | O                           |
| 32ipbabbar01     | 132       | 313         | 286  | −42  | 63         | 0:59:39  | Babbar         | −2:31:47    | O                           |
| 32iprapatr01     | 83        | 281         | 324  | −9   | 38         | 0:29:19  | Ra Patera      | −1:31:07    | O                           |
| 32inthpele01     | 61        | 353         | 255  | −18  | 71         | 0:05:03  | Pele           | −1:00:47    | O                           |
| 32iploki_01      | 44        | 305         | 305  | 14   | 190        | 0:19:13  | Loki           | −0:55:44    | O                           |
| 32inthloki01     | 23        | 303         | 311  | 11   | 85         | 0:11:07  | Loki           | −0:28:26    | O                           |
| 32ispele_01      | 17        | 353         | 262  | −12  | 153        | 0:03:02  | Pele           | −0:17:19    | O                           |
| 32inthpele02     | 11        | 359         | 256  | −17  | 48         | 0:07:05  | Pele           | −0:14:17    | O                           |
| 32iphires01      | 3         | 334         | 287  | −42  | 100        | 0:10:07  | Hi-res S. hem. | −0:08:13    | O                           |
| 32istelgns01     | 1         | 120         | 135  | −65  | 128        | 0:04:03  |                | 0:01:54     | O                           |
| 32intherml01     | 6         | 128         | 129  | −78  | 6          | 0:04:03  |                | 0:05:57     | O                           |
| 32isemakng01     | 8         | 138         | 120  | −23  | 84         | 0:01:27  | Emakong        | 0:09:59     | O                           |
| 32istelgns02     | 9         | 140         | 118  | −44  | 47         | 0:01:41  | Telegonus      | 0:11:27     | O                           |
| 32istohil_01     | 14        | 100         | 159  | −24  | 36         | 0:02:35  | Tohil          | 0:13:08     | O                           |
| 32inemakng01     | 23        | 140         | 119  | −4   | 38         | 0:11:07  | Emakong        | 0:19:05     | O                           |
| 32istupan_01     | 35        | 117         | 145  | −18  | 8          | 0:02:01  | Tupan          | 0:33:15     | O                           |
| 32initupan01     | 40        | 120         | 141  | −18  | 54         | 0:10:07  | Tupan          | 0:35:16     | O                           |
| 32istvasht01     | 49        | 137         | 126  | 62   | 26         | 0:02:01  | Tvashtar       | 0:45:23     | O                           |
| 32inichaac01     | 54        | 115         | 148  | 12   | 11         | 0:10:07  | Chaac          | 0:47:24     | O                           |
| 32isgshbar01     | 61        | 167         | 97   | 16   | 2          | 0:02:21  | Gish Bar       | 0:57:31     | O                           |
| 32inpromth01     | 72        | 133         | 133  | 41   | 12         | 0:13:09  | Prometheus     | 1:01:33     | O                           |
| 32istermin01     | 81        | 103         | 164  | −18  | 6          | 0:02:48  | Terminator     | 1:14:42     | O                           |
| 32istermin02     | 83        | 116         | 152  | 34   | 14         | 0:02:08  | Terminator     | 1:17:30     | O                           |
| 32ipewscan01     | 95        | 134         | 132  | −1   | 74         | 0:14:09  | EW scan        | 1:21:47     | 27                          |
| 32ippolday01     | 212       | 136         | 146  | 47   | 31         | 0:30:20  | Regional       | 2:53:47     | 27                          |
| 33ipdrkmap01     | 1992      | 329         | 108  | 0    | 0          | 0:13:09  | Global         | −9:11:06    | O                           |
| 33ippromth01     | 66        | 38          | 156  | −2   | 6          | 0:20:13  | Prometheus     | −1:04:50    | O                           |
| 33ipewscan01     | 45        | 21          | 175  | 0    | 3          | 0:05:03  | Equator scan   | −0:39:34    | O                           |
| 33ipmarduk01     | 35        | 350         | 210  | −28  | 30         | 0:10:07  | Marduk         | −0:34:30    | O                           |

## 2.1. Data reduction

Each PPR observation was corrected for internal temperature drifts by subtracting a fixed DN value from each sample that was equal to the DN measured when observing dark sky, either during that observation or during a nearby observation, so that sky level was zero in the corrected data. These corrections typically changed calculated brightness temperatures by less than 4 K. For raster scan data, we then created surface temperature maps with maximum possible resolution and S/N by projecting the PPR field of view onto the surface of the target for each sample time, and averaging the DNs in all overlapping fields of view at each location on the

map. For 1-D scans we simply averaged DNs in overlapping fields of view along the scan direction. Finally, we converted the DNs to brightness temperatures, using algorithms developed during pre-launch calibration of PPR. Brightness temperature maps shown here are superposed on the appropriate portions of a global map of Io based on Galileo SSI images (McEwen et al., 1998a). Our experience is that PPR pointing accuracy is approximately 1 mrad compared to the 2.5 mrad instrument field of view, so only small corrections to the reported pointing are usually needed. Pointing is refined if necessary by reference to known volcanic features shown on the SSI-based base maps.

## 2.2. Daytime data

During I31, PPR obtained its first global daytime temperature map with good resolution (31IPDGTM\_01, better than 300 km). For the most part, the  $27\ \mu\text{m}$   $T_B$  distribution follows the expected pattern (Fig. 1) with  $T_B$  peaking near the subsolar point.

Hot spots are not obvious in this map, due to the relatively low resolution (300 km) and the relatively long wavelength. While some of the anomalously hot areas may be related to hotspots (Camaxtli at  $16^\circ\text{ N}$ ,  $137^\circ\text{ W}$  and Tupan at  $18^\circ\text{ S}$ ,  $141^\circ\text{ W}$ ), other areas, such as  $25^\circ\text{ S}$ ,  $130^\circ\text{ W}$  are not associated with known hotspots or any obvious albedo feature. In

the absence of volcanic hot spots, surface temperatures are controlled by the passive re-radiation of sunlight. Thermal inertia variations can have a significant effect on daytime temperatures on a relatively rapidly-rotating, cold object like Io (Spencer et al., 1989; Veeder et al., 1994) and may explain the non-volcanic anomalies (both high and low temperature) in the temperature distribution. On I27 we mapped a smaller area near the volcano Prometheus at  $17\ \mu\text{m}$  at somewhat higher resolution (Fig. 2), and saw similar local temperature patterns, though absolute brightness temperatures are higher than for the same region in Fig. 1 because the local time is closer to noon, and because  $T_B$  increases with decreasing wavelength (Spencer et al., 2003).

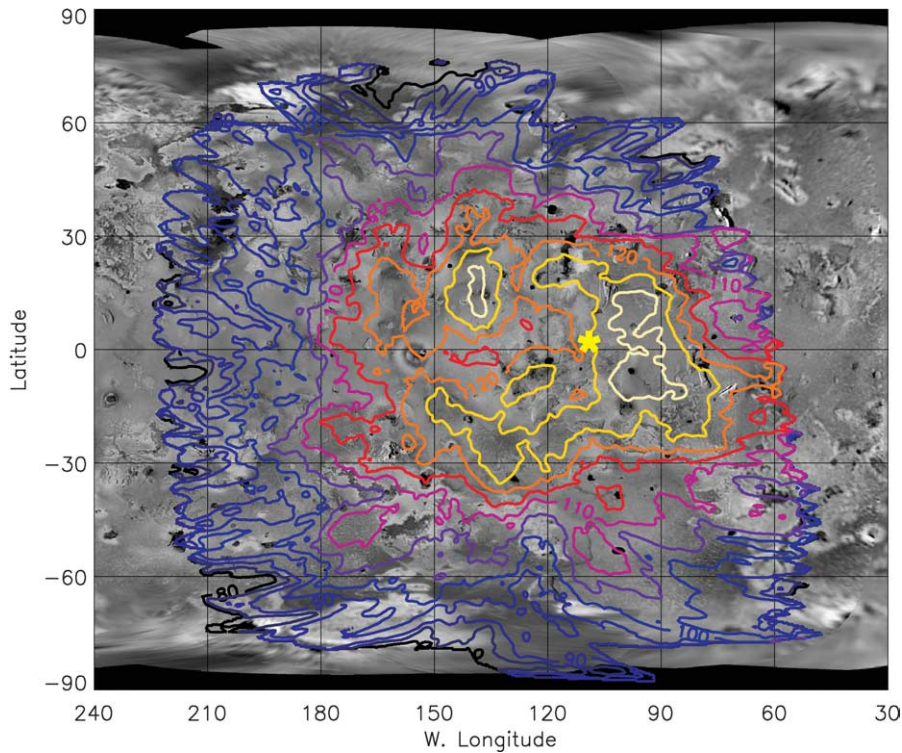


Fig. 1. Map of daytime brightness temperature in the PPR  $27\ \mu\text{m}$  filter, superimposed on an SSI map of Io, from the 31IPDGTM\_01 observation. Contour interval is 5 K. Approximate location of the subsolar point is marked with an \*.

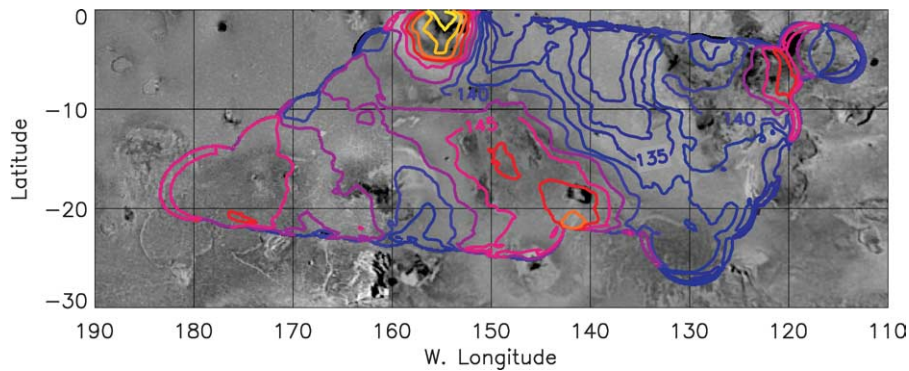


Fig. 2. Daytime equatorial brightness temperatures near the Prometheus volcano in the PPR  $17\ \mu\text{m}$  filter, from the 27IPFROST\_01 observation. Contour interval is 2.5 K. Brightness temperatures may be higher than passive surface kinetic temperatures due to the relatively short wavelength of the observation, as discussed in the text.



### 2.3. Nighttime data

Galileo obtained global nighttime temperature maps in the open filter during I27, I31, and I32; the I31 observation having the best resolution (223 km). Regional maps with higher resolution were made during I27, I31, and I32, giving near-complete coverage of nightside temperatures at 200–100 km resolution. Figure 3 shows a composite temperature map using the highest resolution available from all observations. Galileo generally viewed only the Jupiter-facing hemisphere at night; so all maps include only longitudes in the range 150°–360° W. Due to the improved resolution over most parts of this image, many hotspots can be seen, including some not previously detected by Galileo. Hotspot names and locations are determined by identifying the Patera from the USGS map that corresponds to the PPR hotspot.

Hotspots include: Loki, Amaterasu, Dazhbog, Daedalus, Babbar, Prometheus, Pele, Marduk, Lei-Kung, Reiden, Kurdalagon, Svarog, and Ulgen (Table 2). Two bright but previously unknown north polar hot spots at 290° W, 76° N (corresponding to a prominent dark spot in SSI images, now called Vivasvant Patera) and 245° W, 70° N (now called Chors Patera) were seen in the 31IPNPOLRG01 observation only, but may have been present in other observations which had inadequate spatial resolution to resolve them. There is a striking paucity of bright hot spots in the longitude range 160°–200° W.

While most of the hotspots are clearly point sources even at regional scale resolution, there are two notable exceptions: the enormous lava flows at Lei-Kung Fluctus from 230° W, 55° N to 210° W, 45° N, seen in I27, I31, and I32 global and northern regional maps, and Lerna Regio, at 290° W, 60° S, seen in the 32IPBABBAR01 regional map. Comparison of relatively low-resolution images from Voyager and Galileo implies that both flows fields were emplaced before the Voyager encounter, and were therefore at least 21–22 years old when observed by PPR. Both of these flows are located at high latitude. Recent observations (Marchis et al., 2002; Howell et al., 2001; Lopes-Gautier et al., 1999) have suggested that high-latitude eruptions on Io tend to be less frequent but larger than those at low latitudes, and the presence of these very large, still-warm lava flows at high latitudes is consistent with this pattern. Figure 4 shows a high resolution nighttime scan from I31 taken across Lei-Kung Fluctus. High temperatures correspond to the dark flows in the SSI basemap, as expected. Much of the southern part of the Lei-Kung flow has a nighttime temperature of 135 K, as warm as peak daytime passive temperatures, making it unlikely that the high nighttime temperature of Lei-Kung is due to an unusually high thermal inertia—such high nighttime temperatures almost certainly require an endogenic source. Also note that even at these mid-latitudes, background temperatures are 95 K, about the same as seen near

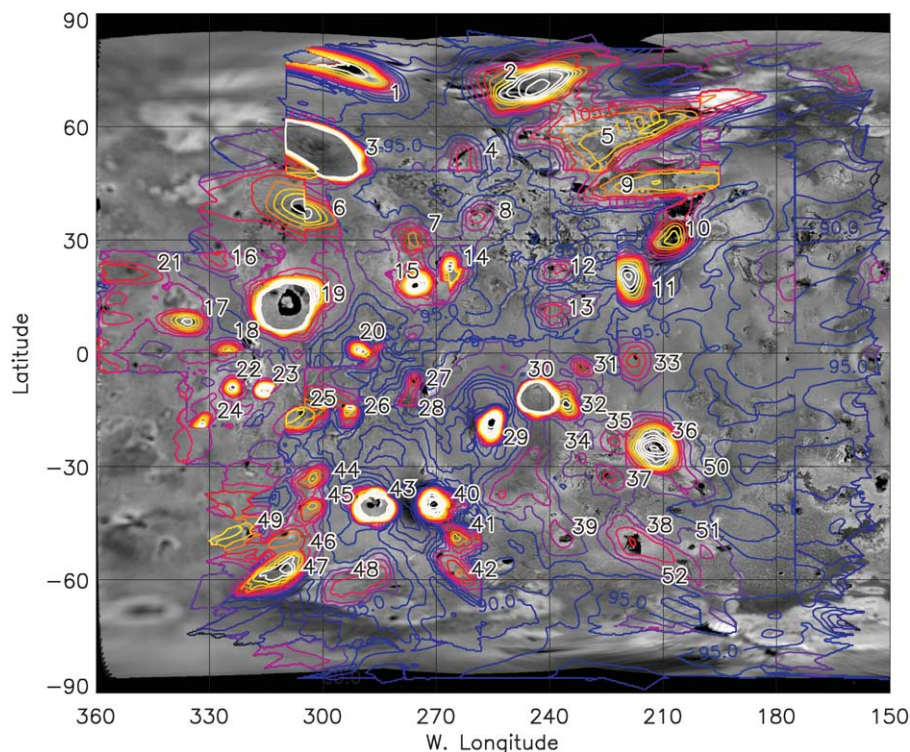


Fig. 3. Map of nighttime effective temperature in PPRs open filter, superimposed on an SSI map of Io. The temperature map is a composite of the highest-resolution global and regional observations from orbits I25, I27, I31, and I32, and shows artifacts at the boundaries between observations. Hot spots observed near Io's limb are elongated perpendicular to the limb when projected onto the map. Contour interval is 2.5 K, and contours above 130 K are omitted to avoid hiding the sources of the brightest hot spots. Hotspots are labeled with numbers that correspond to those listed in Table 2. The map includes data from 25IPGLOBAL01; 27IPLOKI\_01; 31IPNPOLRG; 31IPPELEDK01; 32IPBABBAR01; 32IPCOLCHS01; 32IPRAPATR01; and 32IPREGION01.

Table 2  
Hotspots and power output detected by PPR

| Name of hotspot        | #  | Power output ( $10^{12}$ W) |      |      |      |      |      |      |      |      |      |      | Max/Min |
|------------------------|----|-----------------------------|------|------|------|------|------|------|------|------|------|------|---------|
|                        |    | 25                          | 27a  | 27b  | 31a  | 31b  | 31c  | 32a  | 32b  | 32c  | 32d  | 32e  |         |
| Vivasvant              | 1  | ND                          | ND   | NI   | NI   | NI   | 0.27 | NI   | NI   | NI   | NI   | NI   |         |
| Chors                  | 2  | ND                          | ND   | NI   | ND   | NI   | 0.24 | 0.4  | NI   | NI   | NI   | NI   | 1.67    |
| Dazhbog                | 3  | 0.64                        | ND   | NI   | 3.59 | NI   | Sat  | 4.38 | NI   | 4.24 | NI   | NI   | 6.84    |
| Unnamed, 264° W, 53° N | 4  | ND                          | ND   | NI   | ND   | NI   | 0.15 | ND   | NI   | 0.04 | NI   | NI   | 3.75    |
| North Lei-Kung         | 5  | ND                          | ND   | NI   | ND   | NI   | R    | 0.45 | NI   | ND   | NI   | NI   |         |
| Amaterasu              | 6  | 0.92                        | 0.91 | NI   | 0.91 | NI   | NI   | 0.88 | NI   | NI   | NI   | NI   | 1.05    |
| Atar                   | 7  | ND                          | ND   | NI   | ND   | NI   | NI   | ND   | NI   | 0.13 | NI   | NI   |         |
| Unnamed, 261° W, 37° N | 8  | ND                          | ND   | NI   | 0.11 | NI   | NI   | ND   | NI   | 0.08 | NI   | NI   | 1.38    |
| South Lei-Kung         | 9  | ND                          | ND   | NI   | ND   | NI   | NI   | 0.45 | NI   | R    | NI   | NI   | 1.25    |
| Isum                   | 10 | ND                          | ND   | NI   | 0.44 | NI   | NI   | ND   | NI   | NI   | NI   | NI   |         |
| Mulungu +Susannoo      | 11 | 0.23                        | 0.40 | NI   | 0.43 | NI   | NI   | 0.42 | R    | NI   | NI   | NI   | 1.87    |
| Girru                  | 12 | ND                          | ND   | NI   | 0.11 | NI   | NI   | 0.19 | 0.16 | 0.14 | NI   | NI   | 1.73    |
| Llew                   | 13 | ND                          | ND   | NI   | 0.15 | NI   | NI   | 0.18 | 0.17 | 0.12 | NI   | NI   | 1.5     |
| Shakuru                | 14 | ND                          | ND   | 0.08 | ND   | NI   | NI   | ND   | NI   | ND   | NI   | NI   |         |
| Daedalus               | 15 | R                           | R    | R    | 1.79 | NI   | NI   | 1.43 | NI   | 1.07 | NI   | NI   | 1.67    |
| Fuchi                  | 16 | ND                          | NI   | NI   | NI   | NI   | NI   | NI   | NI   | NI   | NI   | NI   |         |
| Acala                  | 17 | ND                          | NI   | 0.19 | NI   | NI   | NI   | NI   | NI   | NI   | NI   | NI   |         |
| Tol-Ava                | 18 | ND                          | ND   | 0.08 | NI   | NI   | NI   | NI   | NI   | NI   | NI   | NI   |         |
| Loki                   | 19 | 9.9                         | 17.5 | R    | 15.2 | NI   | NI   | NI   | NI   | NI   | NI   | NI   | 1.77    |
| Hephaestus             | 20 | ND                          | ND   | 0.08 | 0.40 | NI   | NI   | 0.39 | NI   | NI   | NI   | NI   | 5       |
| Tiermes                | 21 | NI                          | NI   | NI   | NI   | NI   | NI   | NI   | NI   | NI   | NI   | NI   |         |
| Ra                     | 22 | 0.29                        | ND   | NI   | NI   | NI   | NI   | NI   | NI   | NI   | NI   | 0.06 |         |
| Mazda Catena           | 23 | ND                          | ND   | NI   | NI   | NI   | NI   | NI   | NI   | NI   | NI   | NI   |         |
| Huo Shen               | 24 | ND                          | ND   | NI   | NI   | NI   | NI   | NI   | NI   | NI   | NI   | NI   |         |
| Mihir                  | 25 | ND                          | ND   | NI   | ND   | NI   | NI   | ND   | NI   | NI   | 0.18 | NI   |         |
| Gibil                  | 26 | ND                          | ND   | NI   | ND   | NI   | NI   | ND   | NI   | NI   | 0.13 | NI   |         |
| Unnamed, 277° W, 7° S  | 27 | ND                          | ND   | NI   | ND   | 0.05 | NI   | ND   | NI   | NI   | NI   | NI   |         |
| Unnamed, 278° W, 13° S | 28 | ND                          | ND   | NI   | ND   | 0.03 | NI   | ND   | NI   | NI   | NI   | NI   |         |
| Pele                   | 29 | NI                          | 0.29 | NI   | 0.27 | 0.25 | NI   | 0.28 | 0.35 | NI   | NI   | NI   | 1.4     |
| Pillan                 | 30 | NI                          | 2.55 | NI   | 2.54 | 2.17 | NI   | 1.48 | 1.55 | NI   | NI   | NI   | 1.72    |
| Unnamed, 233° W, 4° S  | 31 | ND                          | ND   | NI   | ND   | 0.04 | NI   | ND   | ND   | NI   | NI   | NI   |         |
| Reiden                 | 32 | NI                          | ND   | NI   | ND   | 1.85 | NI   | ND   | NI   | NI   | NI   | NI   |         |
| Ot                     | 33 | ND                          | ND   | NI   | 0.59 | NI   | NI   | 0.18 | 0.13 | NI   | NI   | NI   | 4.54    |
| Unnamed, 233° W, 28° S | 34 | NI                          | ND   | NI   | ND   | 0.04 | NI   | ND   | NI   | NI   | NI   | NI   |         |
| Unnamed, 224° W, 24° S | 35 | NI                          | ND   | NI   | ND   | 0.04 | NI   | ND   | NI   | NI   | NI   | NI   |         |
| Marduk                 | 36 | NI                          | 0.84 | NI   | 0.46 | NI   | NI   | 0.65 | NI   | NI   | NI   | NI   | 1.83    |
| Wayland                | 37 | NI                          | ND   | NI   | ND   | 0.05 | NI   | ND   | NI   | NI   | NI   | NI   |         |
| Kurdalagon             | 38 | NI                          | 0.44 | NI   | 0.23 | 0.15 | NI   | ND   | NI   | NI   | NI   | NI   | 2.93    |
| Unnamed, 236° W, 49° S | 39 | NI                          | ND   | NI   | ND   | 0.12 | NI   | ND   | NI   | NI   | NI   | NI   |         |
| Babbar                 | 40 | NI                          | 0.47 | NI   | 0.33 | 0.50 | NI   | 0.48 | NI   | NI   | 0.40 | NI   | 1.52    |
| Svarog                 | 41 | NI                          | ND   | NI   | ND   | 0.2  | NI   | ND   | NI   | NI   | 0.14 | NI   | 1.43    |
| Mithra                 | 42 | NI                          | ND   | NI   | ND   | ND   | NI   | ND   | NI   | NI   | 0.08 | NI   |         |
| Ulgen                  | 43 | NI                          | NI   | NI   | 0.68 | 0.34 | NI   | 0.88 | NI   | NI   | 0.73 | NI   | 2.59    |
| Sengen                 | 44 | NI                          | NI   | NI   | NI   | NI   | NI   | NI   | NI   | NI   | 0.16 | NI   |         |
| Rarog                  | 45 | NI                          | ND   | NI   | NI   | NI   | NI   | NI   | NI   | NI   | 0.12 | NI   |         |
| Aten                   | 46 | NI                          | NI   | NI   | NI   | NI   | NI   | NI   | NI   | NI   | ND   | NI   |         |
| Heno                   | 47 | NI                          | ND   | NI   | NI   | NI   | NI   | NI   | NI   | NI   | 0.25 | NI   |         |
| Lerna                  | 48 | NI                          | ND   | NI   | NI   | NI   | NI   | NI   | NI   | NI   | R    | NI   |         |
| Argos                  | 49 | NI                          | ND   | NI   | NI   | NI   | NI   | NI   | NI   | NI   | NI   | NI   |         |
| Rata                   | 50 | NI                          | ND   | NI   | ND   | NI   | NI   | NI   | NI   | NI   | NI   | NI   |         |
| Gabija                 | 51 | NI                          | ND   | NI   | ND   | ND   | NI   | NI   | NI   | NI   | NI   | NI   |         |
| Unnamed, 206° W, 55° S | 52 | NI                          | ND   | NI   | ND   | ND   | NI   | NI   | NI   | NI   | NI   | NI   |         |

NI indicates that the hotspot was not completely in the field imaged, ND indicates that the hotspot was not detected, R indicates that the hotspot was resolved and the power could not be measured with our method, and Sat indicates that the hotspot saturated the detector. If a hotspot was detected more than once, the ratio between the highest and lowest power output is given as "Max/Min." The second column gives the # corresponding to the locations of hotspots shown on Fig. 3. The second row indicates the observation: 25 is for 25ipglobal01 taken on 11/25/1999 at 22:50:04; 27a is for 27ipdrkmap01 taken on 2/22/2000 at 6:56:52; 27b is for 27iploki\_01 taken on 2/22/2000 at 11:18:45; 31a is for 31ipglobal01 taken on 8/6/2001 at 12:15:41; 31b is for 31ippeledk01 taken on 8/6/2001 at 1:56:48; 31c is for 31ipnolrg01 taken on 8/6/2001 at 2:57:24; 32a is for 32ipdrkmap02 taken on 10/15/2001 at 19:13:50; 32b is for 32ipcolchs01 taken on 10/15/2001 at 20:48:53; 32c is for 32ipregion taken on 10/15/2001 at 21:49:33; 32d is for 32ipbabbar01 taken on 10/15/2001 at 23:49:52; and 32e is for 32iprapatr01 taken on 10/15/2001 at 23:50:53.

the equator, suggesting little dropoff of temperature with latitude.

Note that we cannot discount the possibility that the Lerna flow is warm at night due to high thermal inertia rather than release of endogenic heat, as peak nighttime temperatures at PPR resolution are only 103 K. Daytime observations of this flow, which PPR did not obtain, would be required to resolve the ambiguity. However Voyager IRIS observed Lerna Regio in daylight in 1979, and PPR/IRIS comparisons may provide clues to the nature of Lerna Regio.

Nighttime passive temperatures are in the range 90–100 K, but with significant local variations. Temperatures are unusually low (near 86 K) in the inner ejecta blanket of Pele (#29), and in the ejecta from Babbar (#40). These are both unusual low-albedo deposits, where low temperatures might plausibly be due to low thermal inertias caused by fine pyroclastic particles with poor grain-to-grain thermal conductivity (Wechsler et al., 1972). However, similar low temperatures are found in a region centered at 284° W, 25° S, which is a quite different-looking terrain of lava flows where a low thermal inertia may be less likely. There is also a well-defined high temperature (100 K) ring around Pele, about 5 K warmer than surrounding regions, which corresponds in position to the outer reddish-orange ring of Pele's plume deposits seen in visible wavelength images (McEwen et al., 1998a). This could be due to unusually high thermal inertia (caused, for instance, by sintering of particles in the ejecta blanket by condensing gas), or conceivably could result from surface heating by plume infall or condensation. Using the plume SO<sub>2</sub> column density measured by HST in October 1999 ( $7 \times 10^{16}$  cm<sup>-2</sup>, Spencer et al., 2000b), a plume ejection/impact speed of 1.1 km sec<sup>-1</sup> (Spencer et al., 1997), a plume radius of 500 km, and an SO<sub>2</sub> latent heat of condensation of 24.92 kJ mol<sup>-1</sup> (Dean, 1992), we estimate that a 95.0 K surface would be heated to 95.25 K by the mechanical energy of impact of the SO<sub>2</sub> gas, and to 95.16 K by release of latent heat, if the SO<sub>2</sub> gas condensed on hitting the surface. These effects are too small to explain the observed 5 K temperature increase, but are not completely negligible. Mechanical heating could explain the anomaly if, for instance, the plume contained a dust mass much larger than the mass of gas. Arguing against plume heating as a cause of the warm ring is the fact that the plume is known to be highly variable (e.g., McEwen and Soderblom, 1983; Spencer et al., 1997), but the magnitude of the thermal anomaly was similar during all three orbits (I27, I31, I32) in which Pele was mapped. Colchis Regio also shows large temperature variations that do not appear to be associated with low albedo regions (which normally suggest hotspots) and are likely to be due to thermal inertia variations.

Following the method of Spencer et al. (2000a), we can obtain a crude estimate of Io's global volcanic heat flow from these data by assuming that all nighttime emission above a model background temperature is volcanic. Following their method, we assume that passive nighttime temperatures have

a  $\cos^{1/4}$  (latitude) dependence with a temperature of 95 K at the equator. In 31IPGLOBAL01, 38% of Io is covered, and we obtain a global mean heat flow of 2.6 W m<sup>-2</sup> if we assume that the area covered by PPR is representative of the entire area of Io, or 2.0 W m<sup>-2</sup> if we assume that Loki is unique and count its heat flow contribution only once. In the mosaic in Fig. 3, 50% of the satellite is covered, and the global mean heat flow is calculated to be 2.4 or 2.1 W m<sup>-2</sup> if Loki is unique. Spencer et al. (2000a) found, using I25 and I27 PPR data which covered 45% of the surface, a heat flow of 2.0 and 1.7 W m<sup>-2</sup> if Loki is unique.

Figure 5 shows a high resolution scan from I27 taken across Loki Patera. The high temperatures correspond to the dark Loki caldera. Temperatures in the southwest corner of the Patera are approximately 265 K, while those in the eastern portion are 285 K. This matches the lower-resolution I27 PPR Loki data presented in Spencer et al. (2000a) and Howell et al. (2001) and analyzed in Rathbun et al. (2002); as well as data presented in Marchis et al. (2001). This is a very different temperature distribution as that seen at Loki Patera during I24 (Spencer et al., 2000a; Rathbun et al., 2002). The data support the conclusions of Rathbun et al. (2002) that a resurfacing wave travels counter clockwise around Loki. Beyond the edge of the Patera, temperatures drop quickly, but not immediately, to 95 K. Based on comparison of data of this region at different resolutions, we believe that this slight rise in temperature, which extends for roughly six degrees beyond the edge of the caldera, is due to scattered light. Besides this ramp, the background temperature shows very little spatial variability even at 15 km resolution, suggesting that unresolved small hot spots do not contribute significantly to this temperature, as it would be unlikely that the hot spot contribution would be similar in each 15 km field of view.

#### 2.4. Diurnal and latitudinal temperature variations

Daytime temperatures on Io drop away from the subsolar point, as expected (Fig. 1). We also expect to see temperatures change as a function of the time of day and nighttime temperatures to drop at high latitudes. For surfaces in thermal equilibrium with instantaneous sunlight or diurnally-averaged sunlight, both night and day temperatures should vary as  $\cos^{1/4}$  (latitude), though intermediate thermal inertias can produce more complex latitudinal dependences. Following low-resolution nighttime maps from I27 which showed remarkably constant nighttime temperatures with latitude, during I31 PPR took high resolution (60 km) temperature scans from pole to pole during the day (31IPNSSTRP\_01) and from the equator to the southern pole at night (31IPNSDRK\_01) to look more closely at latitudinal temperature variations. Figure 6 shows these scans, binned to the PPR field of view, along with the size and location of the fields of view.

Also shown are both scans on the same plot with  $\cos^{1/4}$  (latitude) curves for comparison. Note that hotspots contam-



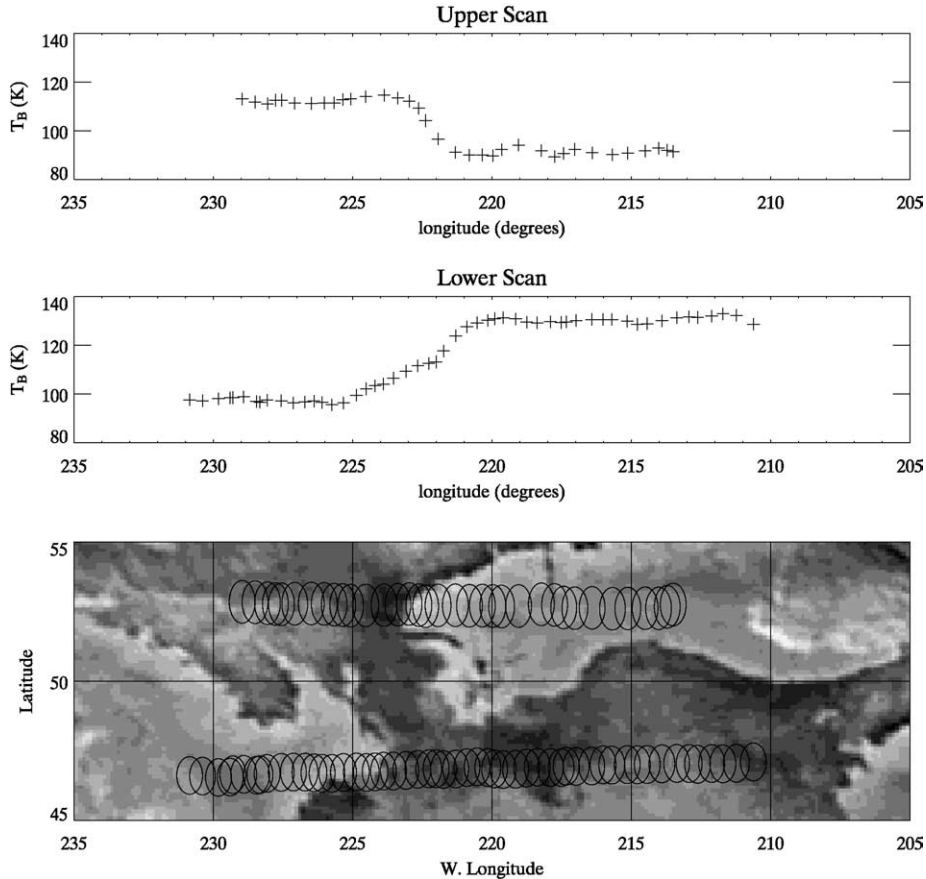


Fig. 4. Nighttime temperature scan across Lei-Kung Fluctus, in the open filter. The top two plots show effective temperature as a function of longitude while the bottom plot shows the location and size of the PPR fields of view overlaid on an SSI image mosaic. Data from 3IIPLEKNG01.

inate the data. The daytime temperatures match the theoretical curve fairly well, except at high latitudes where data are less reliable. The nighttime temperatures exhibit a small but definite dropoff at high latitude, but much less than expected from a  $\cos^{1/4}$  law. The most likely explanation for the surprisingly warm nighttime poles is that excess endogenic heat is being emitted from the polar regions.

Figure 7 shows equatorial background temperature as a function of time of day from several observations. Again, the daytime temperatures from this diurnal temperature curve match our expectations, with temperatures rising after sunrise (90) and dropping after noon (180). Temperatures appear to drop during the night, but only modestly (about 5 K). One possible explanation for the small temperature drop during the night, along with the surprisingly small variation in nighttime temperature with latitude, is that nighttime temperatures are *everywhere* dominated by endogenic heat and that re-radiated sunlight is negligible on the night side, leading to a very high global heat flow of up to  $13.5 \text{ W}$  (Matson et al., 2001). However, given Io's known bolometric albedo of about 0.52 (Simonelli et al., 2001), measurement of Io's total thermal radiation shows that this heat flow is implausibly high (McEwen et al., 2003). That nighttime temperatures between obvious hot spots are dominated by re-radiated sunlight can also be seen from the thermophysical model

fits (Spencer et al., 1989) to the diurnal curve shown in Fig. 7, which use the Simonelli et al. (2001) albedo of 0.52. A homogeneous surface with a thermal inertia of  $7 \times 10^4 \text{ erg cm}^{-2} \text{ s}^{-1/2} \text{ K}$  matches the diurnal variation, but laterally-inhomogeneous models with similar surface coverage of dark, low thermal inertia and bright, high thermal inertia components provide a better match to the slow nighttime cooling. A mixture of somewhat dark low thermal inertia pyroclastic dust and bright, sintered,  $\text{SO}_2$  frost would be one way to produce such a laterally inhomogeneous surface, and similar inhomogeneous thermophysical models have been invoked previously (Sinton and Kaminski, 1988; Veeder et al., 1994). We also show an inhomogeneous model in which background surface temperatures have been increased by an endogenic heat flow of  $1 \text{ W m}^{-2}$ , for instance by conduction through the crust or widespread low-temperature hot spots. It is clear that background equatorial heat flows much larger than  $1 \text{ W m}^{-2}$  would not be consistent with observed temperatures, given the known bolometric albedo, and that Io's observed heat flow of about  $2 \text{ W m}^{-2}$  is therefore dominated by the obvious large hot spots (which we avoided in Fig. 7), not by background heat flow.

Even the inhomogeneous thermophysical models in Fig. 7 predict greater nighttime cooling than is inferred from the observations. Perhaps the surface is even more inhomoge-

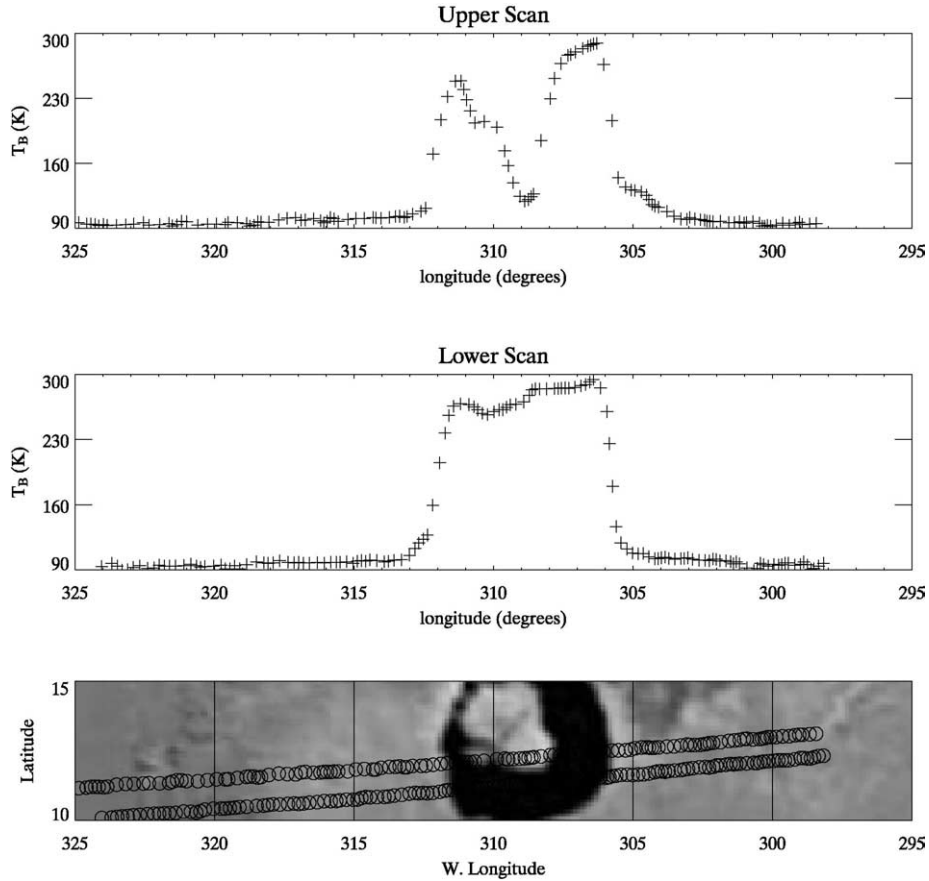


Fig. 5. Nighttime temperature scan across Loki Patera. The top two plots show brightness temperature as a function of longitude while the bottom plot shows the location and size of the PPR fields of view overlaid on an SSI image mosaic. Data from 27IPLOKI\_03.

neous than the models, or perhaps the regions that PPR scanned early in the night have intrinsically lower nighttime temperatures (due to thermal inertia or albedo variations) than those scanned later in the night.

### 2.5. Frost temperatures and atmospheric pressure

The daytime brightness temperatures can be compared to surface  $\text{SO}_2$  frost temperatures inferred from the pressure of  $\text{SO}_2$  in the atmosphere. Recent HST UV spectroscopy of the anti-jovian hemisphere, centered on the Prometheus volcano, found peak  $\text{SO}_2$  column densities for a low-latitude region near the subsolar point, centered at  $8^\circ \text{ N}$ ,  $162^\circ \text{ W}$ , of  $2.5 \times 10^{17} \text{ cm}^{-2}$  (Jessup et al., 2004). If supported by vapor pressure equilibrium with surface frost, the inferred subsolar  $\text{SO}_2$  frost temperature is near 119 K (Wagman, 1979). However,  $27 \mu\text{m}$  low-latitude subsolar temperatures (Figs. 6, 7) peak near 130 K, even in our highest resolution (60 km) observations which are the least likely to be contaminated by unresolved hotspots. Most likely, even the highest-resolution PPR fields of view contain unresolved regions with varying passive temperatures. The  $\text{SO}_2$  frost areal coverage is usually less than 100% at Galileo NIMS resolution (Douté et al., 2001), and it is likely that the frost occupies cold traps, smaller than 60 km in extent, within each PPR field of view.

The cold frost temperatures are likely to be due to some combination of high albedo and high effective thermal inertia (due for instance to grain growth and sintering (Douté et al., 2001) or solid-state greenhouse effects (Matson and Brown, 1989)), which will suppress daytime temperatures while enhancing nighttime temperatures.

### 2.6. Hotspot power output

Many hotspots can be seen in the nighttime global and regional temperature maps and most are unresolved. When they are unresolved, it is easy to calculate the total power output from the hotspot by simply measuring the peak effective temperature of the unresolved hotspot ( $T_p$ ), the background temperature near the hotspot ( $T_a$ ), and the area of the projected PPR field of view ( $A$ ), and assuming the surface radiates as a blackbody with unit emissivity so that  $P = \sigma A(T_p^4 - T_a^4)$ , where  $\sigma$  is the Stefan–Boltzman constant. Table 2 shows the calculated power output for the hotspots seen in maps from I25, I27, I31, and I32. Errors in measuring the temperatures and areas of the hotspots lead to variations of less than  $0.05 \text{ W m}^{-2}$  however, if the entire hotspot does not lie in a single field of view, we may be underestimating the power output by much more. Variations of a single hotspot in images taken during the same

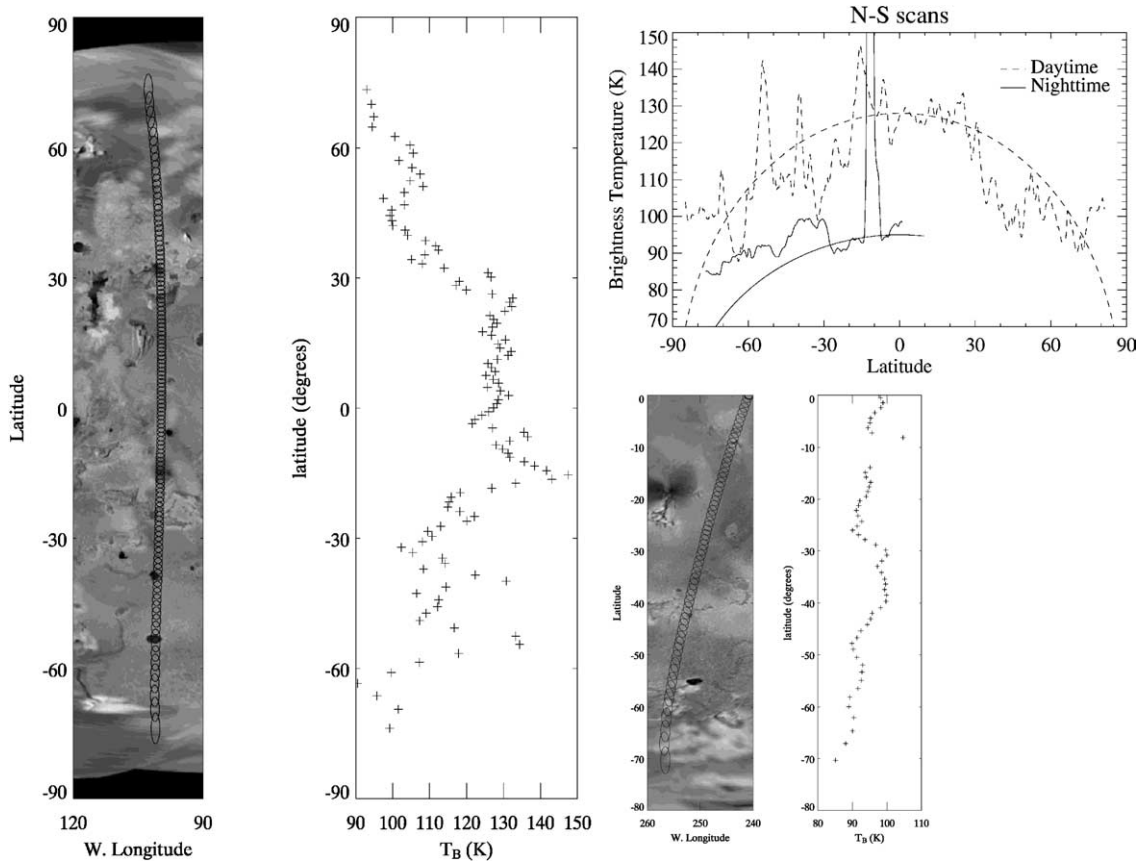


Fig. 6. Temperature variation with latitude. Temperature scans across Io taken during the day (31IPNSSTRP01, left) and at night (31IPNSDRK\_01, lower right). Next to the scans are plots which show the location and size of the PPR fields of view overlaid on an SSI image mosaic. The plot in the upper right shows both temperature scans and  $\cos^{1/4}$  functions to compare the temperature drop at high latitudes with the expected drop.

orbit are likely to be due to errors. In cases where the same hotspot was seen more than once, we also calculate the ratio between the maximum and minimum power calculated, noted on the table as “Max/Min.” This should give us an idea of how changeable these hotspots are. The most dramatic changes occurred at Dazhbog ( $303^\circ$  W,  $55^\circ$  N), where faint thermal emission was seen in I25, but it was dramatically brighter during I31 and I32, approaching the brightness of Loki, which is generally by far the brightest area on Io at these mid-infrared wavelengths (Spencer et al., 2000a). This implies that the eruption of the pyroclastic deposits around Dazhbog seen by SSI during I31 was associated with extensive lava flows (McEwen et al., 2003). Pillan, where a major eruption was first observed in June 1997 (McEwen et al., 1998b) gradually decreased in flux, probably due to cooling of the 1997 lava flows. Loki also goes through significant changes, though since it is usually located near the limb and is often resolved, its power is more complicated to measure.

### 3. Conclusions

We have tabulated all of the data taken by PPR at Io during the 1999–2002 close encounters, and presented some

scientific highlights from this rich data set. These data give a very detailed characterization of nightside temperatures with near-complete coverage at better than 200 km resolution. The better resolution nightside data show a modest poleward drop in background temperatures, though not as rapid as the expected  $\cos^{1/4}$  (latitude), perhaps indicating excess endogenic emission near the poles. Background temperatures at low latitudes, however, are dominated by re-radiated sunlight. The data show passive nighttime thermal anomalies in many places, notably in the Pele pyroclastic deposits. Many hotspots can be seen, their power output measured and compared at different times from different orbits. Large flux increases were seen at Dazhbog. Only two large, extended, hotspots were found, Lei-Kung Fluctus and Lerna Regio, which appear to be pre-Voyager lava flows.

Only one good (300 km resolution) global daytime temperature map was obtained (31IPDGTM\_01). Unlike the nighttime temperatures, daytime temperatures vary strongly, and in the expected manner, with both latitude and local time. Comparison of high spatial resolution temperature measurements with observed daytime  $\text{SO}_2$  gas pressures on Io provides evidence for local cold trapping of  $\text{SO}_2$  frost on scales smaller than the 60 km resolution of the PPR data.

In this paper we have just begun analysis of this large and fascinating data set. We hope that our presentation of the data

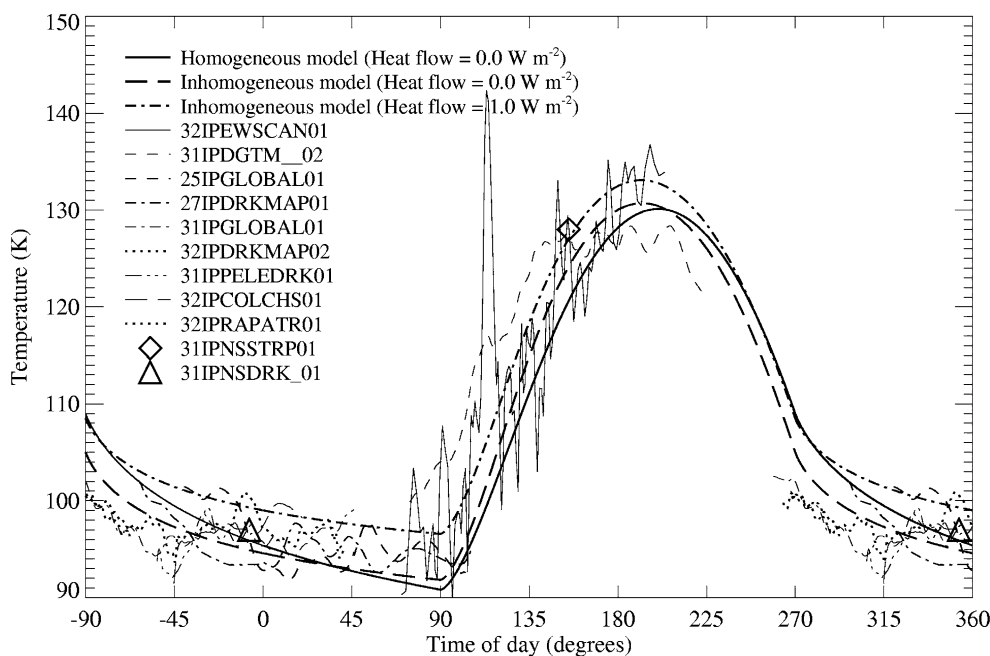


Fig. 7. Diurnal temperature variations. Measurements of temperature as a function of time of day taken from several observations are plotted together. Time of day is given as an angle, with 0 at midnight, 90 at sunrise, and 180 at noon. All data are averages taken within 20 degrees of the equator and we have avoided obvious hotspots. The 32IPEWSCAN curve is an exception, as these are not data averaged from a map, but are from a single scan across Io, binned to the PPR field of view. A hotspot (Prometheus at local time 110°) can clearly be seen in this scan. The smooth curves show thermal models matched to the diurnal temperature variations. All have a mean albedo of 0.52, consistent with Io's mean albedo. The homogeneous model has a thermal inertia of  $7 \times 10^4 \text{ erg cm}^{-2} \text{ s}^{-1/2} \text{ K}$ , while the inhomogeneous models have two surface components with equal areal coverage, one with albedo 0.34 and thermal inertia  $4 \times 10^4$ , and the other with albedo 0.70 and thermal inertia  $1 \times 10^6$ . The warmer inhomogeneous model includes an endogenic heat flow of  $1 \text{ W m}^{-2}$ , roughly the maximum background heat flow consistent with the data.

leads to more thorough analysis and more understanding of the processes at work on Io.

## Acknowledgments

We thank the Galileo project and PPR team for acquiring the data. This work was supported by a grant to J.R.S. through the NASA Planetary Geology and Geophysics program, grant # NAG5-10497.

## References

- Carlson, R.W., Weissman, P.R., Smythe, W.D., Mahoney, J.C., NIMS Science and Engineering Teams, 1992. Near infrared spectrometer experiment on Galileo. *Space Sci. Rev.* 60, 457–502.
- Dean, J.A., 1992. *Lange's Handbook of Chemistry*, fourteen ed. McGraw-Hill, New York.
- Douté, S., Schmitt, B., Lopes-Gautier, R., Carlson, R., Soderblom, L., Shirley, J., the Galileo NIMS Team, 2001. Mapping  $\text{SO}_2$  frost on Io by the modeling of NIMS hyperspectral images. *Icarus* 149, 107–132.
- Howell, R.R., 1997. Thermal emission from lava flows on Io. *Icarus* 127, 394–407.
- Howell, R.R., Spencer, J.R., Goguen, J.D., Marchis, F., Prangé, R., Fusco, T., Blaney, D.L., Veeder, G.J., Rathbun, J.A., Orton, G.S., Grocholski, A.J., Stansberry, J.A., Kanner, G.S., Hege, E.K., 2001. Ground-based observations of volcanism on Io in 1999 and early 2000. *J. Geophys. Res.* 106, 33129–33140.
- Jessup, K.L., Spencer, J.R., Ballester, G.E., Howell, R.R., Roesler, F., Vigel, M., Yelle, R., 2004. The atmospheric signature of Io's Prometheus plume and anti-jovian hemisphere: evidence for a sublimation atmosphere. *Icarus* 169, 197–215.
- Khanna, R.K., Pearl, J.C., Dahmani, R., 1995. Infrared spectra and structure of solid phases of sulfur trioxide: possible identification of solid  $\text{SO}_3$  on Io's surface. *Icarus* 115, 250–257.
- Lopes-Gautier, R., McEwen, A.S., Smythe, W.B., Geissler, P.E., Kamp, L., Davies, A.G., Spencer, J.R., Keszthelyi, L., Carlson, R., Leader, F.E., Mehlman, R., Soderblom, L., the Galileo NIMS and SSI Teams, 1999. Active volcanism on Io: global distribution and variations in activity. *Icarus* 140, 243–262.
- Marchis, F., Prangé, R., Fusco, T., 2001. A survey of Io's volcanism by adaptive optics observations in the  $3.9\text{-}\mu\text{m}$  thermal band (1996–1999). *J. Geophys. Res.* 106, 33141–33160.
- Marchis, F., de Pater, I., Davies, A.G., Roe, H.G., Fusco, T., Le Mignant, D., Descamps, P., Macintosh, B.A., Prangé, R., 2002. High-resolution Keck adaptive optics imaging of violent volcanic activity on Io. *Icarus* 160, 124–131.
- Martin, T.Z., Goguen, J.D., Travis, L.D., Tamppari, L.K., Barnard, L., Dose, L., 2000. Galileo PPR polarimetric phase curves for the galilean satellites. *Bull. Am. Astron. Soc.* 32, Abstract 39.4.
- Matson, D.L., Brown, R.H., 1989. Solid-state greenhouses and their implications for icy satellites. *Icarus* 77, 67–81.
- Matson, D.L., Johnson, T.V., Veeder, G.J., Blaney, D.L., Davies, A.G., 2001. Upper bound on Io's heat flow. *J. Geophys. Res.* 106, 33021–33024.
- McEwen, A.S., Soderblom, L.A., 1983. Two classes of volcanic plumes on Io. *Icarus* 55, 191–217.
- McEwen, A.S., Isbell, N.R., Pearl, J.C., 1992. Io thermophysics: new models with Voyager 1 thermal IR spectra. In: *Proc. Lunar. Planet. Sci. Conf.* 23rd. Abstract 881.

- McEwen, A.S., Isbell, N.R., Edwards, K.E., Pearl, J.C., 1996. Temperatures on Io: implications to geophysics, volcanology, and volatile transport. In: *Proc. Lunar Planet. Sci. Conf. 27th*, pp. 843–844. Abstract.
- McEwen, A.S., Keszthelyi, L., Geissler, P., Simonelli, D.P., Carr, M.H., Johnson, T.V., Klaasen, K.P., Breneman, H.H., Jones, T.J., Kaufman, J.M., Magee, K.P., Sensky, D.A., Belton, M.J.S., Schubert, G., 1998a. Active volcanism on Io as seen by Galileo SSI. *Icarus* 135, 181–219.
- McEwen, A.S., Keszthelyi, L., Spencer, J.R., Schubert, G., Matson, D.L., Lopes-Gautier, R., Klaasen, K.P., Johnson, T.V., Head, J.W., Geissler, P., Fagents, S., Davies, A.G., Carr, M.H., Breneman, H.H., Belton, M.J.S., 1998b. High-temperature silicate volcanism on Jupiter's moon Io. *Science* 281, 87–90.
- McEwen, A.S., Keszthelyi, L., Lopes, R., Schenk, P., Spencer, J., 2003. The lithosphere and surface of Io. In: Bagenal, F. (Ed.), *Jupiter*. Cambridge Univ. Press, Cambridge. In press.
- Rathbun, J.A., Spencer, J.R., Davies, A.G., Howell, R.R., Wilson, L., 2002. Loki, Io: a periodic volcano. *Geophys. Res. Lett.* 29, 10.1029/2002GL014747.
- Russell, E.E., Brown, F.G., Chandos, R.A., Fincher, W.C., Kubel, L.F., Lacy, A.A., Travis, L.D., 1992. Galileo photopolarimeter/radiometer experiment. *Space Sci. Rev.* 60, 531–563.
- Simonelli, D.P., Dodd, C., Veverka, J., 2001. Regolith variations on Io: implications for bolometric albedos. *J. Geophys. Res.* 106, 33241–33252.
- Sinton, W.M., Kaminski, C., 1988. Infrared observations of eclipses of Io, its thermophysical parameters, and the thermal radiation of the Loki volcano and environs. *Icarus* 75, 207–232.
- Spencer, J.R., Lebofsky, L.A., Sykes, M.V., 1989. Systematic biases in radiometric diameter determinations. *Icarus* 78, 337–354.
- Spencer, J.R., Sartoretti, P., Ballester, G.E., McEwen, A.S., Clarke, J.T., McGrath, M.A., 1997. Pele plume (Io): observations with the Hubble Space Telescope. *Geophys. Res. Lett.* 24, 2471–2474.
- Spencer, J.R., Rathbun, J.A., Travis, L.D., Tamppari, L.K., Barnard, L., Martin, T.Z., McEwen, A.S., 2000a. Io's thermal emission from the Galileo photopolarimeter–radiometer. *Science* 288, 1198–1201.
- Spencer, J.R., Jessup, K.L., McGrath, M.A., Ballester, G.E., Yelle, R., 2000b. Discovery of gaseous S<sub>2</sub> in Io's Pele plume. *Science* 288, 1208–1210.
- Spencer, J.R., Carlson, R.W., Becker, T., 2003. Appendix: maps and spectra. In: Bagenal, F. (Ed.), *Jupiter*. Cambridge Univ. Press, Cambridge. In press.
- Wagman, D.D., 1979. Sublimation Pressure and Enthalpy of SO<sub>2</sub>. Chem. Thermodyn. Data Center. Natl. Bureau Standards, Washington, DC.
- Wechsler, A.E., Glaser, P.E., Little, A.D., Fountain, J.A., 1972. Thermal properties of granulated materials. In: Lucas, J.W. (Ed.), *Thermal Characteristics of the Moon*. MIT Press, Cambridge, pp. 215–241.
- Veeder, G.J., Matson, D.L., Johnson, T.V., Blaney, D.L., Goguen, J.D., 1994. Io's heat flow from infrared radiometry: 1983–1993. *J. Geophys. Res.* 99, 17095–17162.